

# Physical properties of galaxies at high redshifts II

---

## Different galaxies at high z's

Luminous Infra Red Galaxies (LIRGs):  $L_{\text{FIR}} > 10^{11} L_{\odot}$

Ultra Luminous Infra Red Galaxies (ULIRGs):  $L_{\text{FIR}} > 10^{12} L_{\odot}$

SubMillimeter-selected Galaxies (SMGs):

$L_{\text{FIR}} > 10^{13} L_{\odot}$   $\text{SFR} \gtrsim 1000 M_{\odot} \text{ yr}^{-1}$   
number density  $(2-6) \times 10^{-6} \text{ Mpc}^{-3}$   
The typical gas consumption timescales  $(2-4) \times 10^7 \text{ yr}$

The main question: how quickly the gas is consumed in galaxies at high redshifts. Observations maybe biased to galaxies with very high star formation rates. and thus give a bit biased picture. Motivation: observe galaxies in CO and FIR. Flux in CO is related with abundance of molecular gas. Flux in FIR gives SFR. So, the combination gives the rate of gas consumption.

We present the first detection of molecular gas cooling CO emission lines from ordinary massive galaxies at  $z = 1.5$ . Two sources were observed with the IRAM Plateau de Bure Interferometer, selected to lie in the mass–star formation rate correlation at their redshift, thus being representative of massive high- $z$  galaxies. Both sources were detected with high confidence, yielding  $L'_{\text{CO}} \sim 2 \times 10^{10} \text{ K km s}^{-1} \text{ pc}^2$ . For one of the sources we find evidence of velocity shear, implying CO sizes of  $\sim 10 \text{ kpc}$ . With an infrared luminosity of  $L_{\text{FIR}} \sim 10^{12} L_{\odot}$ , these disklike galaxies are borderline ULIRGs but with star formation efficiency similar to that of local spirals, and an order of magnitude lower than that in submillimeter galaxies. This suggests a CO to total gas conversion factor similar to local spirals, gas consumption timescales approaching 1 Gyr or longer, and molecular gas masses reaching  $\sim 10^{11} M_{\odot}$ , comparable to or larger than the estimated stellar masses. These results support a major role of in situ gas consumption over cosmological timescales and with relatively low star formation efficiency, analogous to that of local spiral disks, for the formation of today's most massive galaxies and their central black holes. Given the high space density of similar galaxies,  $\sim 10^{-4} \text{ Mpc}^{-3}$ , this implies a widespread presence of gas-rich galaxies in the early universe, many of which might be within reach of detailed investigations of current and planned facilities.

We use a conversion rate (Kennicutt 1998)  $L_{\text{FIR}}/L_{\odot} = 0.8 \times 10^{10} \text{SFR} (M_{\odot} \text{ yr}^{-1})$ , adapted to a Chabrier (2003) stellar initial mass function and on the assumption, appropriate for these galaxies, that  $L_{\text{FIR}}$  is about 80% of the bolometric luminosity.

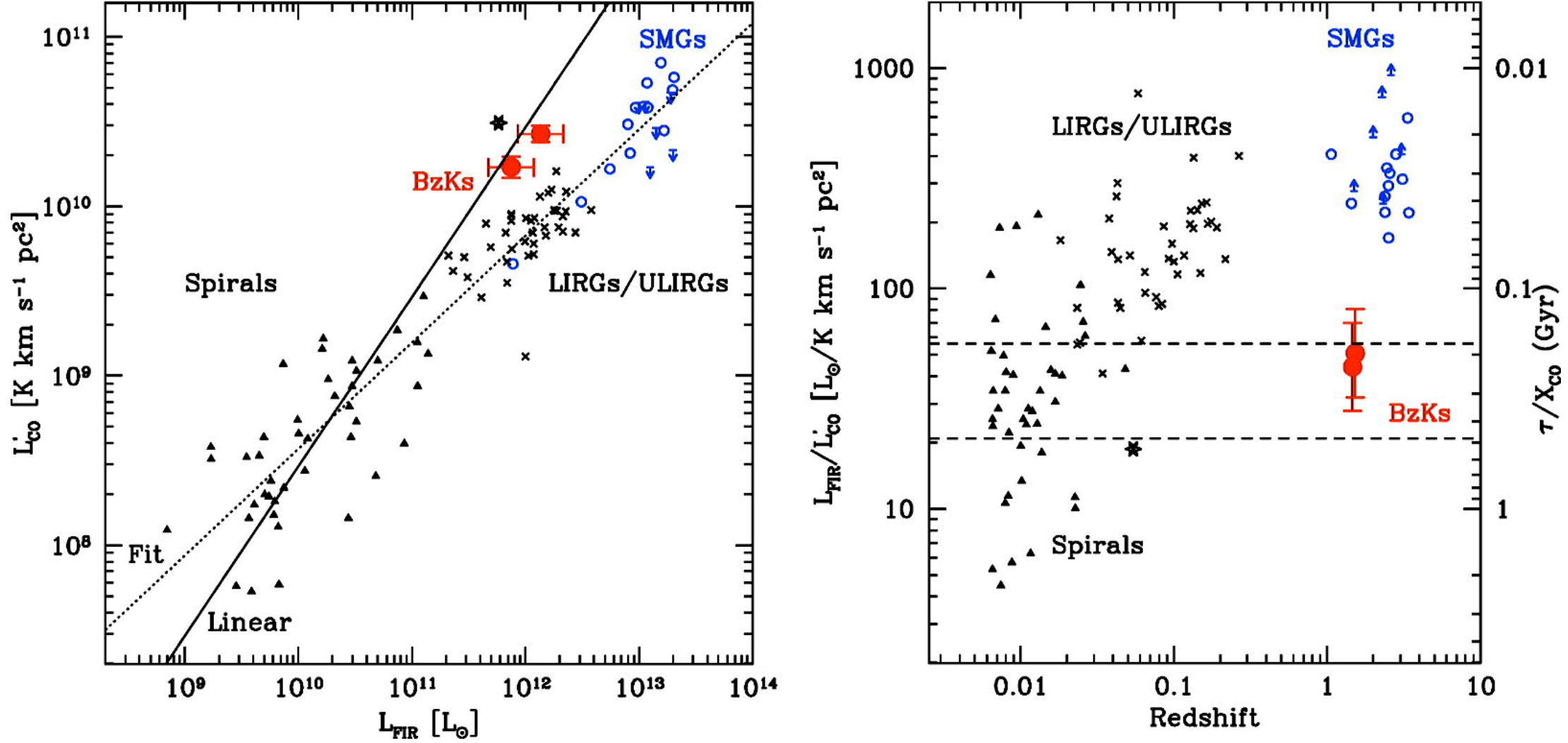


FIG. 3.—Comparison of molecular CO luminosity ( $L'_{\text{CO}}$ ) to far-infrared luminosity ( $L_{\text{FIR}}$ ; integrated between 40 and 500  $\mu\text{m}$ ). Quantities for the two *BzK* galaxies presented in this work are shown as large filled circles. The left panel shows the comparison of the two luminosities. The dotted line is the best-fit relation to spirals (*triangles*), LIRG/ULIRGs (*crosses*), and distant SMGs (*open circles*). The solid line is for a linear  $L'_{\text{CO}}$ -to- $L_{\text{FIR}}$  correlation normalized to the ratio of local spirals. The local LIRG with high  $L'_{\text{CO}}$  content, behaving similarly to distant *BzKs*, is VII Zw 31 (plotted as an asterisk; Downes & Solomon 1998), which interestingly also has fairly cold 60  $\mu\text{m}$ /100  $\mu\text{m}$  color ratios and larger CO size compared to other ULIRGs. The right panel shows the  $L_{\text{FIR}}$ -to- $L'_{\text{CO}}$  ratio as a function of redshift. The dashed horizontal lines show the semi-interquartile range of local spirals.

In order to evaluate the implications of these results for massive galaxy formation, recall that the two observed galaxies are representative of massive galaxies at high redshifts. They were selected for CO observations simply due to the availability of known spectroscopic redshifts. The two galaxies lie on the SFR–to–stellar mass correlation inferred at  $1.4 < z < 2.5$ , and their colors and morphologies are fully typical of massive  $z \sim 2$  galaxies. Star-forming galaxies in that redshift range with similar stellar masses are common in the distant universe, with space densities of the order of  $10^{-4} \text{ Mpc}^{-3}$ , quite a bit larger than the  $(2\text{--}6) \times 10^{-6} \text{ Mpc}^{-3}$  observed for SMGs by Chapman et al. (2003). Clearly, these results point to the existence of a much larger population of gas-rich galaxies in the distant universe than previously thought.

The large molecular gas fraction in these galaxies, possibly up to 50% or more, would likely give rise to large-scale instabilities, with the formation of clumps (e.g., Immeli et al. 2004; Bournaud et al. 2007). This could explain the clumpy structure of these two galaxies, and in general of a large fraction of the high- $z$  massive galaxies (e.g., Daddi et al. 2004a), and the high velocity dispersions observed in many of the high- $z$  massive disk galaxies (e.g., Genzel et al. 2006; Forster Schreiber et al. 2006).

# From Rings to Bulges: Evidence for Rapid Secular Galaxy Evolution at $z \sim 2$ from Integral Field Spectroscopy in the SINS Survey

Genzel et al 2008, ApJ 687, 59

---

We present H $\alpha$  integral field spectroscopy of well-resolved, UV/optically selected  $z \sim 2$  star-forming galaxies as part of the SINS survey with SINFONI on the ESO VLT.

Our laser guide star adaptive optics and good seeing data show the presence of turbulent rotating star-forming outer rings/disks, plus central bulge/inner disk components, whose mass fractions relative to the total dynamical mass appear to scale with the [N II]/H $\alpha$  flux ratio and the star formation age.

We propose that the buildup of the central disks and bulges of massive galaxies at  $z \sim 2$  can be driven by the early secular evolution of gas-rich proto-disks.

High-redshift disks exhibit large random motions. This turbulence may in part be stirred up by the release of gravitational energy in the rapid "cold" accretion flows along the filaments of the cosmic web. As a result, dynamical friction and viscous processes proceed on a timescale of  $< 1$  Gyr, at least an order of magnitude faster than in  $z \sim 0$  disk galaxies.

Early secular evolution thus drives gas and stars into the central regions and can build up exponential disks and massive bulges, even without major mergers. Secular evolution along with increased efficiency of star formation at high surface densities may also help to account for the short timescales of the stellar buildup observed in massive galaxies at  $z \sim 2$ .

Deep surveys have become efficient in detecting  $z=1.5-3.5$  star-forming galaxy populations near the peak of cosmic star formation and QSO activity.

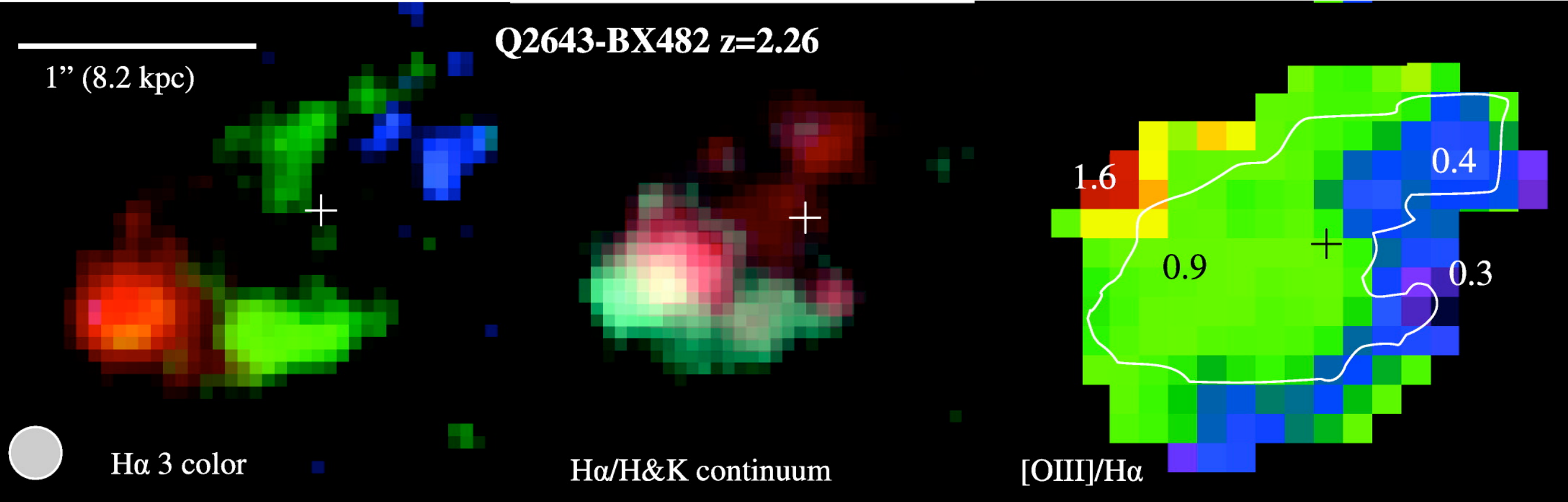
Large samples are now available, based on their rest-frame UV magnitude/color properties or on rest-frame optical magnitude/color properties (“star-forming” or “s”-BzKs). These selection criteria sample fairly luminous ( $10^{11}-10^{12}L_{\odot}$ ) galaxies with star formation rates of  $10-300 M_{\odot} \text{ yr}^{-1}$ , with a range of ages 10 Myr -3 Gyr and stellar masses  $10^9-10^{11.5}M_{\odot}$ .

These galaxies contribute a large fraction of the cosmic star formation activity and stellar mass density at  $z=2$

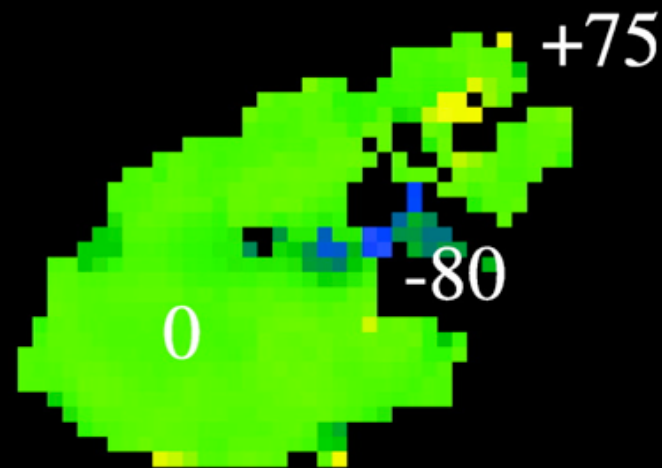
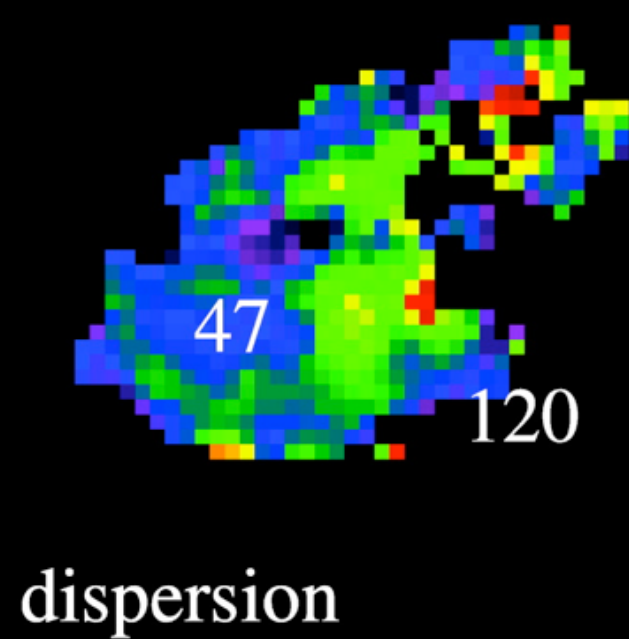
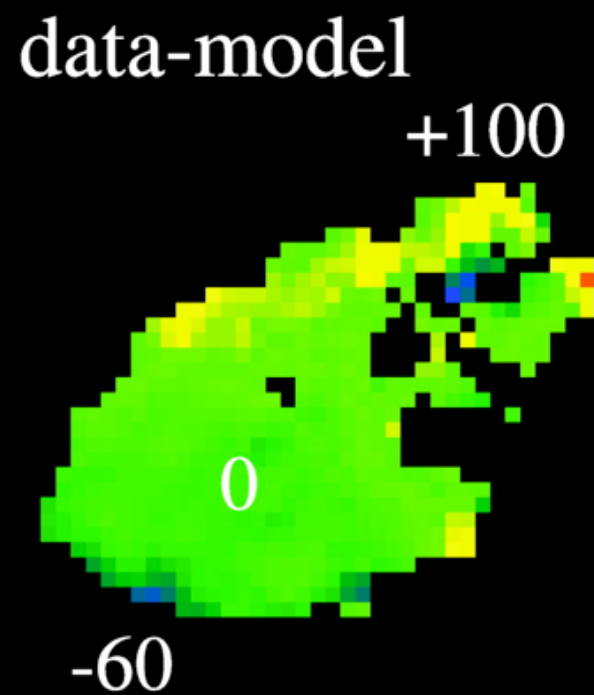
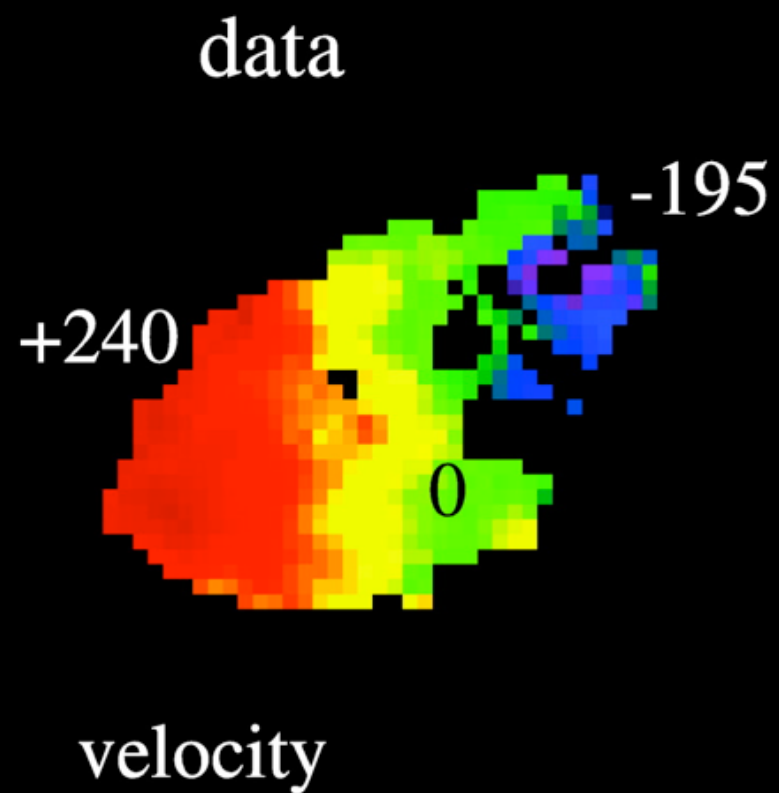
Still to be determined is how these high- $z$  galaxies formed their stars, when and how the first disks and bulges formed, and how their subsequent evolutions relate to each other. Was the star formation history, and especially the formation of bulges, driven by short, intense bursts following major mergers (mass ratios  $<3:1$ )? Or was this evolution dominated by a rapid but more continuous “cold” accretion of gas from the dark matter halos, including large mass ratio ( $\geq 10:1$ ) gas-rich minor mergers

As part of the SINS survey of high- $z$  galaxy kinematics, we observed the  $H\alpha$  and [O III] lines and the rest-frame  $R$ -band continuum in the UV-selected BX galaxy Q2346-BX 482 ( $z=2.26$ ), as well as the  $H\alpha$  line and rest-frame  $R$ -band continuum in the optically selected s-BzK galaxy BzK 6004-3482 ( $z=2.39$ ). In addition we reanalyzed ... other galaxies at  $z\sim 2$ . .... Seeing 0.2-0.5”

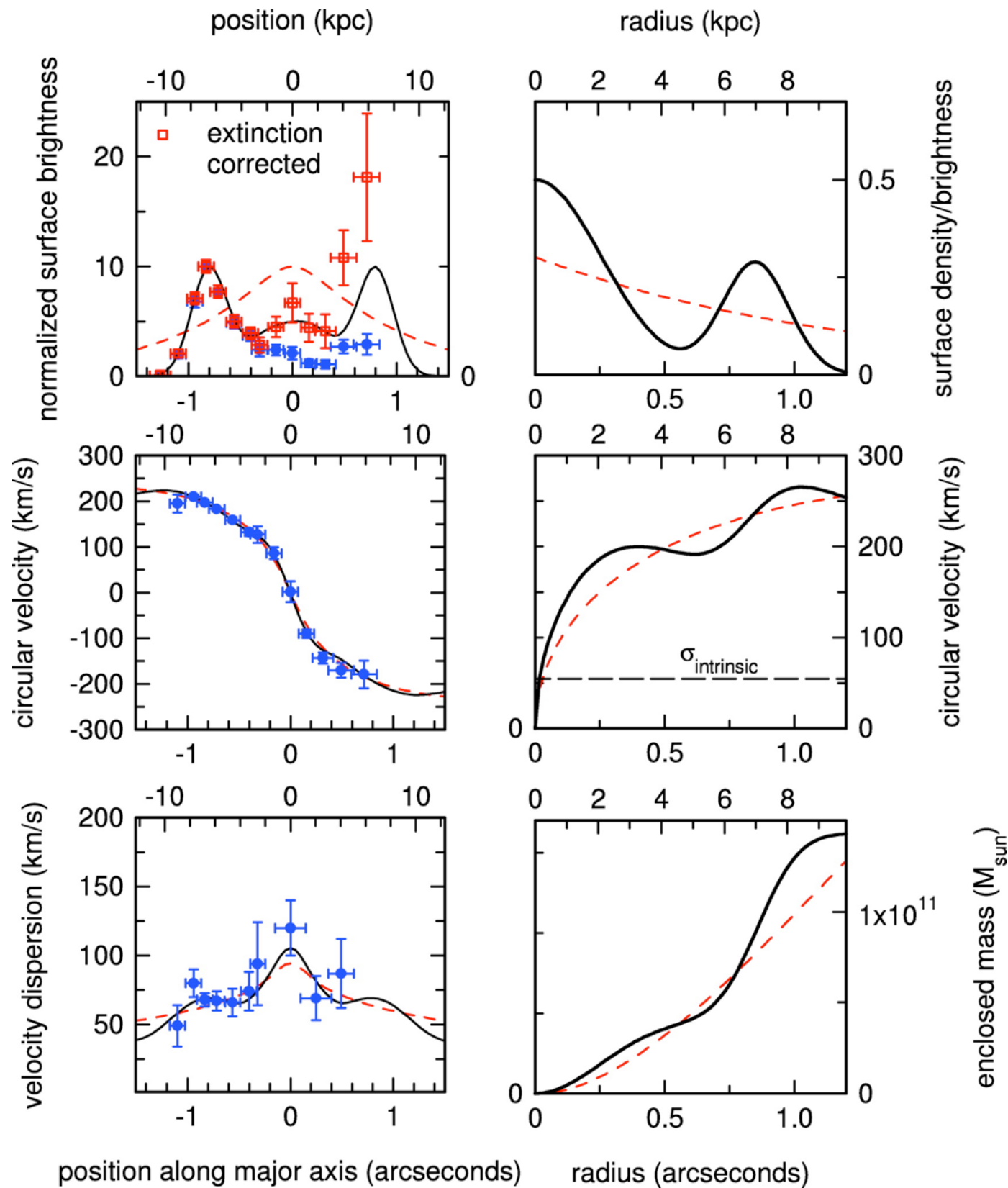
None of these five galaxies show evidence for an ongoing or recent major merger. Their star formation rates nevertheless are quite high.



H $\alpha$ , [O III] line, and  $H$  and  $K$  continuum observations of Q2343-BX 482 ( $z=2.26$ ). *Left*: Three-color composite of blueshifted, central, and redshifted H $\alpha$  line emission, from SINFONI LGSF data at 0.2" FWHM (*shaded circle*). *Middle*: Integrated SINFONI H $\alpha$  emission (*light blue*) superposed on NIC2 H $_{160}$  continuum (*red*) from N. M. Förster Schreiber et al. (2008), with a resolution comparable to the H $\alpha$  data. The images were aligned on the brightest spot in the southeast part of the ring, whose  $K$ -band continuum is also detected in the SINFONI cube. The white cross marks the dynamical center of the object as determined by our modeling.



Two-dimensional H $\alpha$  velocity field and kinematic modeling of BX 482. *Left:* Velocity centroid map (*top*) and velocity dispersion map (*bottom*). *Right:* Residual map (data minus model) of velocity (*top*) and velocity dispersion (*bottom*).



*Left:* Kinematic major axis cuts in projected H $\alpha$  flux (*top*), projected velocity (*middle*), and projected velocity dispersion (*bottom*), along P.A.  $-65^\circ$ . Blue filled circles are the measurements. Vertical-axis bars are the  $\pm 1 \sigma$  errors; horizontal bars denote the aperture size. The black solid lines represent the best-fitting ring+bulge model, and the red dotted lines the best-fitting exponential disk model.

The red squares in the top left panel denote the H $\alpha$  fluxes corrected for screen extinction (see text). *Right:* Radial cuts of the best fitting, ring+bulge (*solid black line*) and exponential (*red dotted line*) model distributions for the enclosed mass (*bottom*), intrinsic rotation curve (*middle*), and mass/brightness distribution (*top*).

The dotted horizontal line in the middle panel marks the level of the intrinsic velocity dispersion in the ring, as derived from the residual velocity distribution.

The velocity and velocity dispersion data are well fit either by a superposition of a fairly narrow ( $0.3''$ ) ring at radius  $0.9''$ , plus a central mass (a bulge or central disk), or by an exponential disk model.

The former model is obviously motivated by the morphology of the H $\alpha$  emission, while latter is the canonical distribution found in low- $z$  disk galaxies. For both models the maximum intrinsic rotation velocity is  $235 \text{ km s}^{-1}$

Derived Properties of the  $z \sim 2$  Star-Forming Galaxies: Part 1

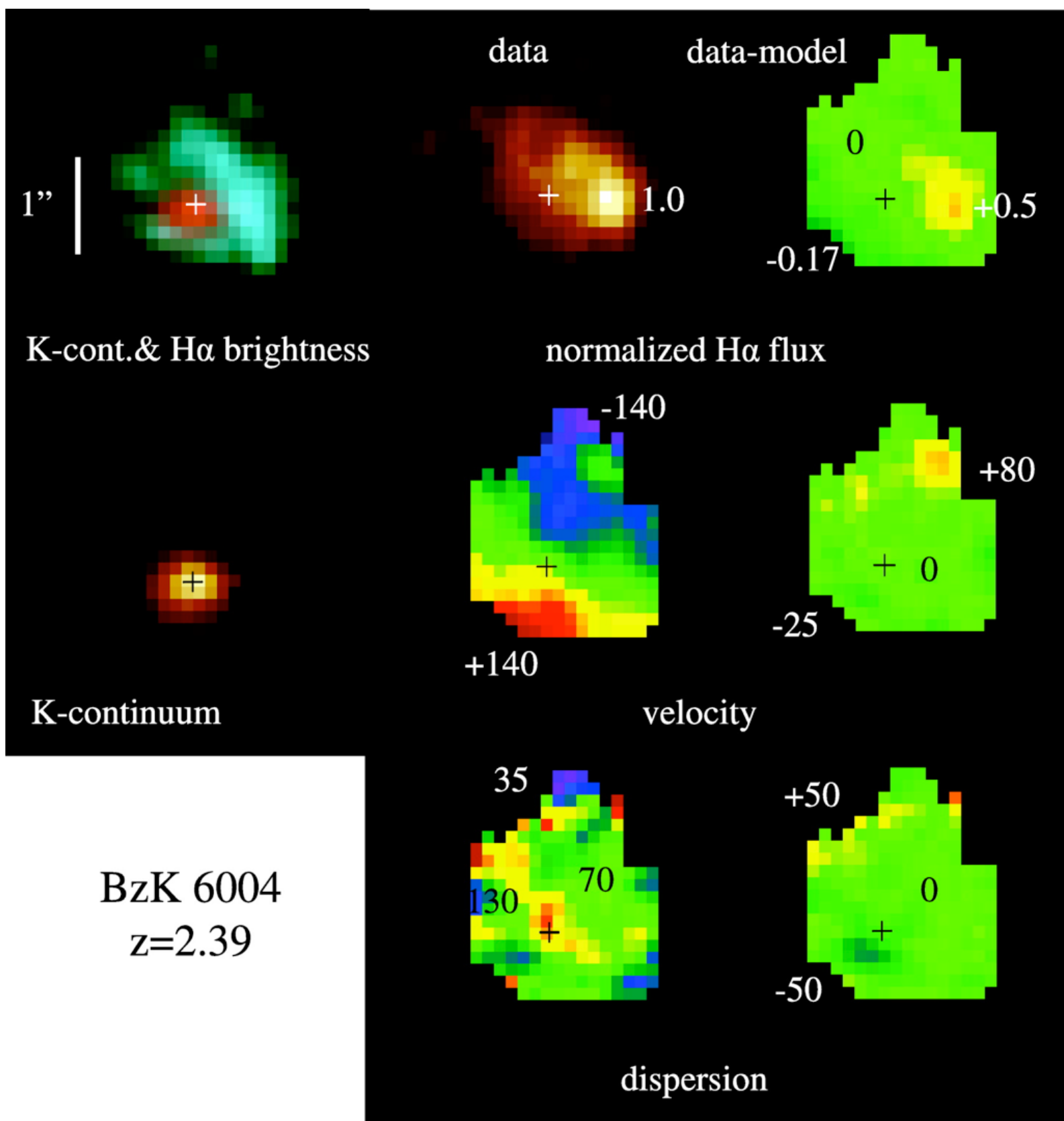
Parameter	MD 41 ( $z = 2.17$ )	BX 482 ( $z = 2.26$ )	BX 389 ( $z = 2.17$ )	BX 610 ( $z = 2.21$ )	BzK 6004 ( $z = 2.39$ )
$R_{\text{ring}}$ (kpc)...	5.9 (0.6)	7.0 (0.8)	4.4 (0.5)	4.4 (0.5)	6.9 (0.8)
Inclination (deg)...	71 (5)	65 (7)	80 (5)	33 (5)	35 (8)
SFR <sup>a</sup> ( $M_{\odot} \text{ yr}^{-1}$ )...	75	140	150	210	160
$M_{\text{dyn}}(\leq 20 \text{ kpc}) (M_{\odot})^{\text{b}}$ ...	$0.7 (0.15) \times 10^{11}$	$1.4 (0.2) \times 10^{11}$	$1.4 (0.2) \times 10^{11}$	$1.5 (0.5) \times 10^{11} \text{ }^{\text{c}}$	$1.9 (0.5) \times 10^{11}$
$M_{*} (M_{\odot})$ ...	$0.17\text{-}0.36 \times 10^{11}$	$0.43\text{-}0.89 \times 10^{11}$	$0.7 (0.2) \times 10^{11}$	$1.7 (0.3) \times 10^{11}$	$5.8 (2) \times 10^{11}$
$M_{\text{gas}} (M_{\odot})^{\text{d}}$ ...	$\sim 0.2 \times 10^{11}$	$\sim 0.3 \times 10^{11}$	$\sim 0.2 \times 10^{11}$	$\sim 0.3 \times 10^{11}$	$\sim 0.3 \times 10^{11}$
$M_{\text{gas}}/M_{\text{dyn}}$ ...	$\sim 0.3$	$\sim 0.2$	$\sim 0.2$	$\sim 0.1$	$\sim 0.1$
$M_{\text{dyn}}(\leq 0.4'')/M_{\text{dyn}}(1.2'')^{\text{e}}$ ...	$\leq 0.15 (3 \sigma)$	0.205 (0.03)	0.39 (0.08)	0.39 (0.08)	0.37 (0.04)
Comments on fit...	exponential disk model produces too centrally concentrated light distribution	exponential disk model produces too centrally concentrated light distribution	exponential disk compatible with data $< 1''$ but produces too much light at $> 1''$	exponential disk compatible with available data to $\sim 1.2''$	exponential disk does not fit central velocity distribution and outer rotation curve

Adopting a constant star formation model with  $0.4Z_{\odot}$  tracks, a Kroupa/Chabrier IMF, and a Calzetti ([2001](#)) extinction model with  $A_V=1.5-2$ , .... we get a mass of live stars of  $(4-9)e10M_{\odot}$  for a plausible age range of 0.3-1 Gyr. Adding this stellar mass and the gas mass estimated from the  $H\alpha$ -based star formation rate and a Kennicutt-Schmidt recipe ( $3e10M_{\odot}$ , [Table 2](#)) results in a baryonic mass of  $(7-12)e10M_{\odot}$  associated with the visible ring (+bulge) structure.

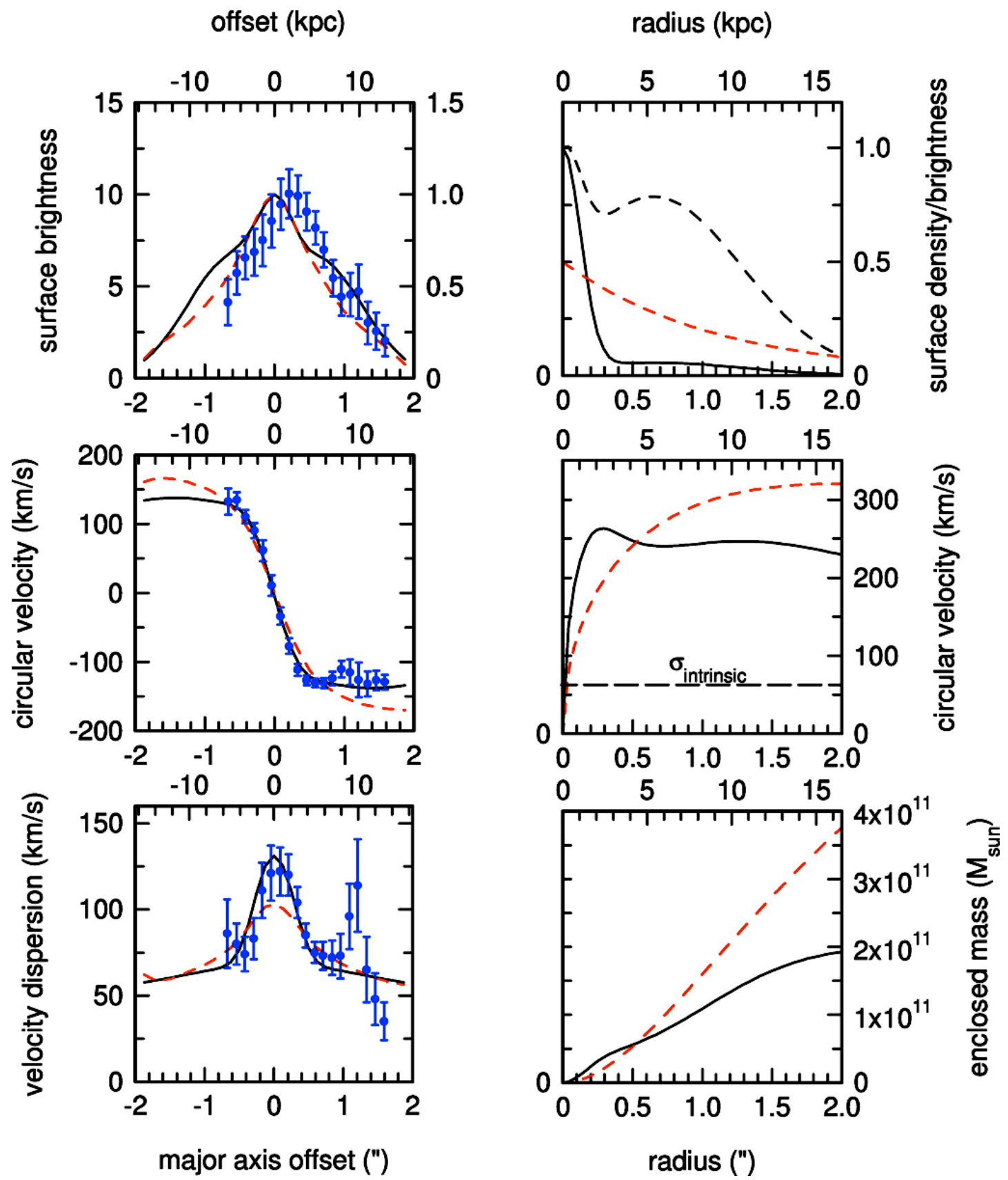
Allowing for a 20%-40% dark matter contribution to the dynamical mass within  $\sim 10-15$  kpc then yields a sum of dark matter and baryonic matter of  $(10-18) e10M_{\odot}$ .

Our dynamical modeling yields a total dynamical mass of  $(14.3\pm 2)e10M_{\odot}$ , leaving little or no space for any additional underlying older stellar distribution that is not traced by our data.

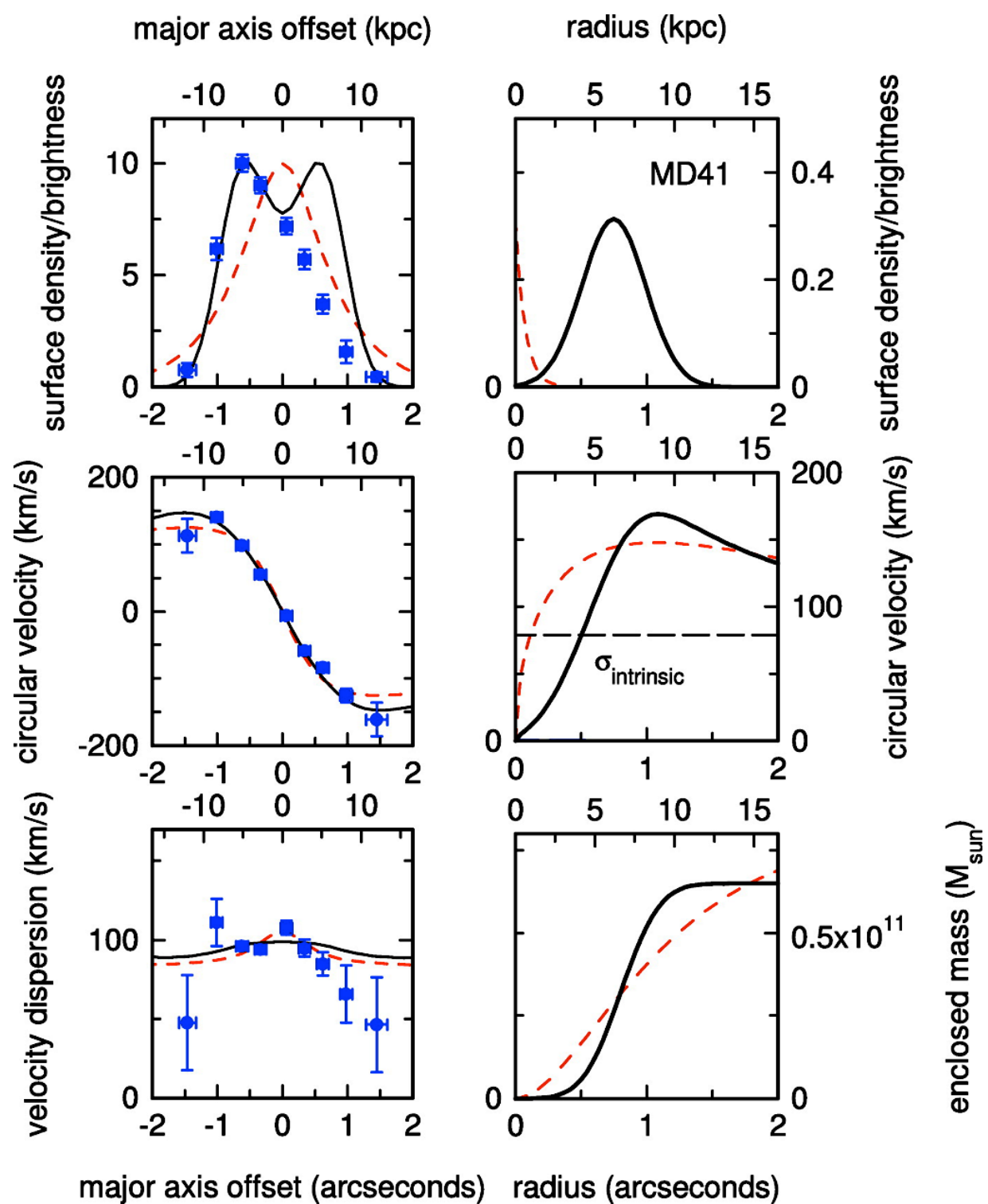
We conclude that the baryonic matter distribution of BX 482 is most likely a ring, plus a small bulge/central disk.



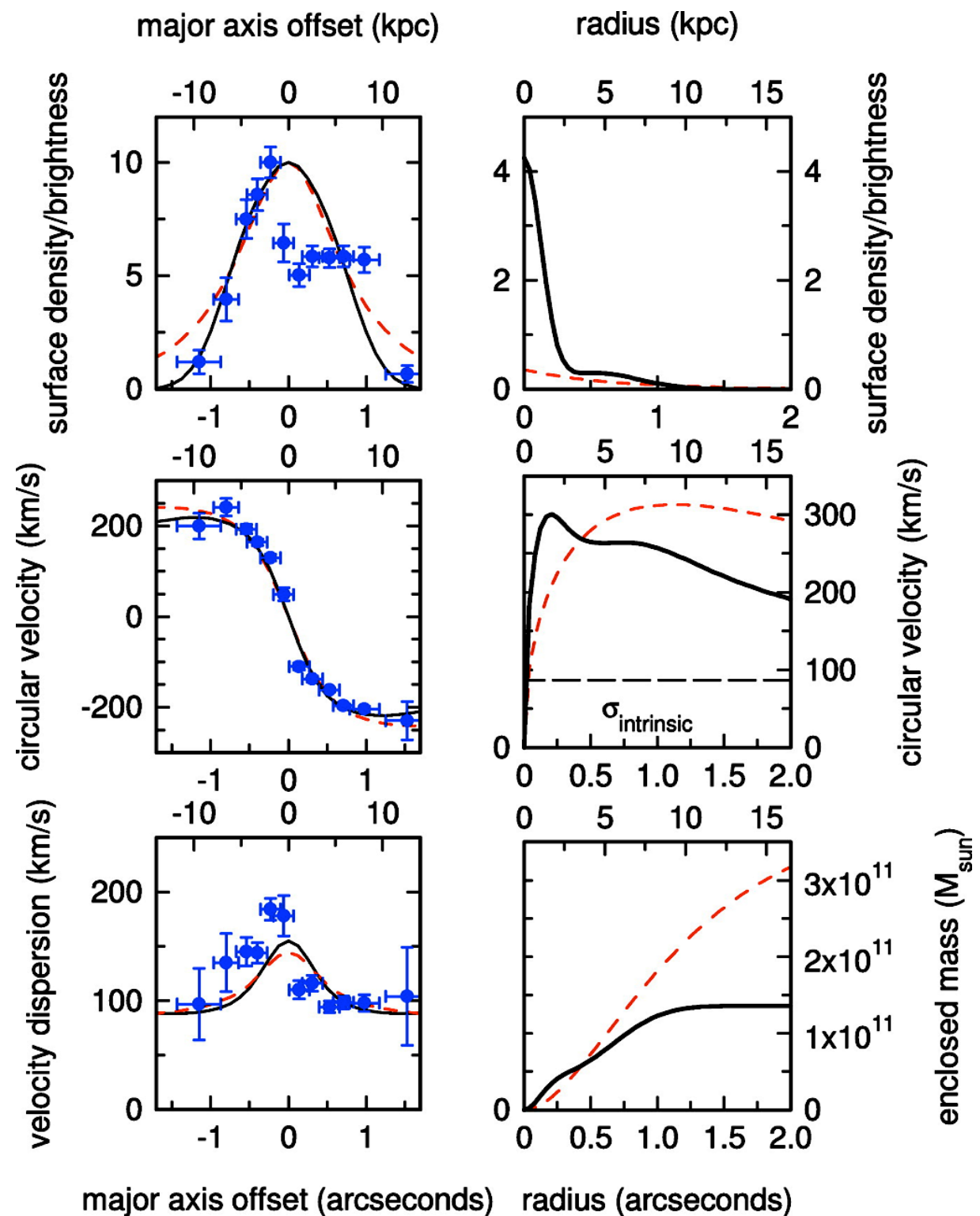
SINFONI LGSF H $\alpha$  data set of D3a6004-3482 ( z=2.39), at a resolution of 0.45" FWHM



H $\alpha$  major axis cuts and kinematic modeling of SSA 22-MD 41 ( $z=2.17$ ) at a resolution of  $\sim 0.5''$  FWHM



H $\alpha$  major axis cuts and kinematic modeling of Q2343-BX 389 ( $z=2.17$ ), at a resolution of  $\sim 0.5''$  FWHM



We fit the H $\alpha$  velocity fields of all galaxies with simple rotating disk models

A specific model requires specifying one or several mass/light components, parameterized by azimuthally symmetric analytic functions (e.g., exponential disks, Gaussians, rings, etc.), the total dynamical mass  $M_{\text{dyn}}$ ,  $z$ -scale height, inclination, position angle of the major axis on the sky, and a component of constant velocity dispersion throughout the disk ( $\sigma_{01}$ ).

A given  $z$ -scale height results in an additional  $z$ -velocity dispersion  $\sigma_{02}$ . In the approximation of a very large and very thin disk, this is given by

$$h_z/R = 0.5(\sigma_{02}/v_d)^2, \quad (1a)$$

where  $v_d$  is the rotation velocity at radius  $R$

The eight actively star-forming galaxies in [Table 3](#) ( $\sim 0.2\text{-}3 M_{\odot} \text{ yr}^{-1} \text{ kpc}^{-2}$ ) all have a large component of random local gas motion, 45-90 km s $^{-1}$ , in agreement with the earlier finding of Förster Schreiber et al. ([2006](#)). Given the spatial and spectral properties of the other  $\sim 50$  galaxies in the SINS survey, this conclusion appears to hold generally for the entire population of  $z=2$  star-forming galaxies

## Turbulent and Clumpy Disks

### Derived Properties of BX/s-BzK Galaxies: Part 2

Parameter	BX 502	MD 41	BX 482	BX 389	ZC 782941	BzK 15504	BX 610	BzK 6004
$v_d$ (km s <sup>-1</sup> )...	75 (25)	175 (30)	235 (40)	265 (40)	285 (30)	230 (30)	290 (70)	255 (40)
$R_d$ (kpc)...	1.7 (0.5)	5.9 (0.6)	7 (0.8)	4.4 (0.5)	3.6 (1)	4.5 (0.8)	4.4 (0.5)	6.9 (0.8)
[N II]/H $\alpha$ ...	0.073 (0.026)	0.08 (0.02)	0.11 (0.026)	0.21 (0.035)	0.24 (0.025)	0.36 (0.04)	0.38 (0.035)	0.42 (0.035)
$M^*/\text{SFR}(\text{H}\alpha)^{\text{a}}$ (Gyr)...	0.04	...	...	0.5	...	0.8	0.8	3.6
$t^*(\text{SED})$ (Gyr)...	0.23 (0.15)	...	...	2.7 (2)	...	1.6 ( $^{+0}_{-1}$ )	2.7 (2)	2.5 ( $^{+0}_{-1.2}$ )
EW(H $\alpha$ ) (Å)...	2200 (550)	>130	...	300 (75)	150 (38)	125 (30)	145 (36)	68 (17)
$\Sigma_{\text{SFR}}^{\text{a}}$ ( $M_{\odot} \text{ yr}^{-1} \text{ kpc}^{-2}$ )...	3.6	0.35	0.57	0.6	1.5	1.2	1.2	0.6
$\sigma_0$ (km s <sup>-1</sup> )...	77 (10)	79 (10)	55 (5)	87 (10)	88 (15)	45 (5)	60 (7)	60 (7)
$v_d/\sigma_0$ ...	1 (0.4)	2.2 (0.7)	4.3 (0.8)	2.9 (0.7)	3.2 (0.6)	5.1 (0.7)	4.8 (0.8)	4.3 (1.5)

the star formation age,  $M^*/\text{SFR}$ , is relatively small

Essentially the entire dynamical mass in the central 0.4" of all sources must be baryonic:

As a first-order estimate, consider a Navarro, Frenk, & White (1997) dark matter distribution with concentration parameters of Bullock et al. (2001), with a disk angular momentum parameter of  $\lambda=0.1$  and with a disk mass fraction (relative to the halo) of  $m_d = \lambda$ , set by the requirement of gravitational instability of the disk (Mo et al. 1998).

With these assumptions, the range of maximum disk rotation velocities in Table 2 corresponds to halo circular velocities of  $190 \pm 70 \text{ km s}^{-1}$  and dark matter mass contribution of  $10^{9.9} M_\odot$  within 3 kpc of the center. This mass corresponds to 5%-10% of the dynamical masses we infer in Table 2.

The dark matter contributions to the *total* dynamical masses in Table 2 are larger. For the same assumptions as above, the dark matter mass contributions within the disk/ring radii ( $\sim 6$  kpc) are about 20%, and within 10 kpc they are about 40% of the total dynamical masses.

## *Turbulent and Clumpy Disks*

The Jeans length in a gravitationally unstable gas disk with  $Q_{\text{gas, Toomre}} \ll 1$  is

$$L_{\text{Jeans}} = \frac{\pi}{\sqrt{2}} \left( \frac{\sigma_0}{v_d} \right) R_r Q_{\text{Toomre}}, \quad (2)$$

which yields  $L_{\text{Jeans}} = 2.5$  kpc or  $0.3''$  for the parameters appropriate for the galaxies in Tables [2](#) and [3](#). The observed sizes of the giant H $\alpha$  clumps/star forming complexes in the clumpy galaxies are consistent with the Jeans lengths inferred from the galaxies' kinematics properties. The H $\alpha$  clumps thus may be initially close to virial equilibrium.

it is clear that the star formation complexes must be very massive (see also Elmegreen & Elmegreen [2005](#)),

$$M_c = \frac{L_c^2 v_d^2}{4GR_d} \sim 10^{9.4 \pm 0.5} M_\odot. \quad (3)$$

These masses are obviously much larger than even the most massive H II regions in starburst galaxies ( $10^7$ - $10^8 M_\odot$ ).

Once fragmentation and star formation sets in (, [eq. \[2\]](#)), the secular evolution timescale is then given by the dynamical friction timescale of the clumps against the background of the disk/halo. Based on Chandrasekhar's formula, the dynamical friction timescale is

$$t_{df} = \beta \left( \frac{R}{\lambda_{\text{Jeans}}} \right)^2 t_{\text{dyn}}(R) = \beta \left( \frac{v_d}{\sigma_0} \right)^2 t_{\text{dyn}}(R), \quad (6)$$

with an (uncertain) dimensionless factor (see above references). Here  $t_{\text{dyn}}$  is the dynamical timescale,

$t_{\text{dyn}} = 2.4 \times 10^7 R_6 / v_{250}$  yr,  $R_6$  is the disk radius in units of 6 kpc, and  $v_{250}$  is the disk circular velocity in units of 250 km s<sup>-1</sup>.

Disk galaxies at  $z=0$  have  $v_d/\sigma = 10-20$  (e.g., Dib et al. [2006](#)) and secular processes proceed on a timescale of several Gyr or more (Kormendy & Kennicutt [2004](#)).

The star-forming galaxies we study here are clearly different. In these galaxies,  $v_d/\sigma$  ranges between 1 and 5. Compared to  $z=0$ , gaseous and stellar processes proceed faster by at least one order of magnitude or more,

$$\begin{aligned} t_{\text{sec}}(z \sim 2) &\sim 10-30 t_{\text{dyn}}(R) \sim 0.5 \text{ Gyr} \\ &\sim t_{\text{dyn}}(R_{\text{vir}}) \sim 0.2 t_H(z \sim 2). \end{aligned} \quad (7)$$

## MULTI-WAVELENGTH VIEW OF KILOPARSEC-SCALE CLUMPS IN STAR-FORMING GALAXIES AT $z \sim 2$

Yicheng Guo, Mauro Giavalisco, Henry C. Ferguson, Paolo Cassata, and Anton M. Koekemoer *ApJ* 757, 120, 2012

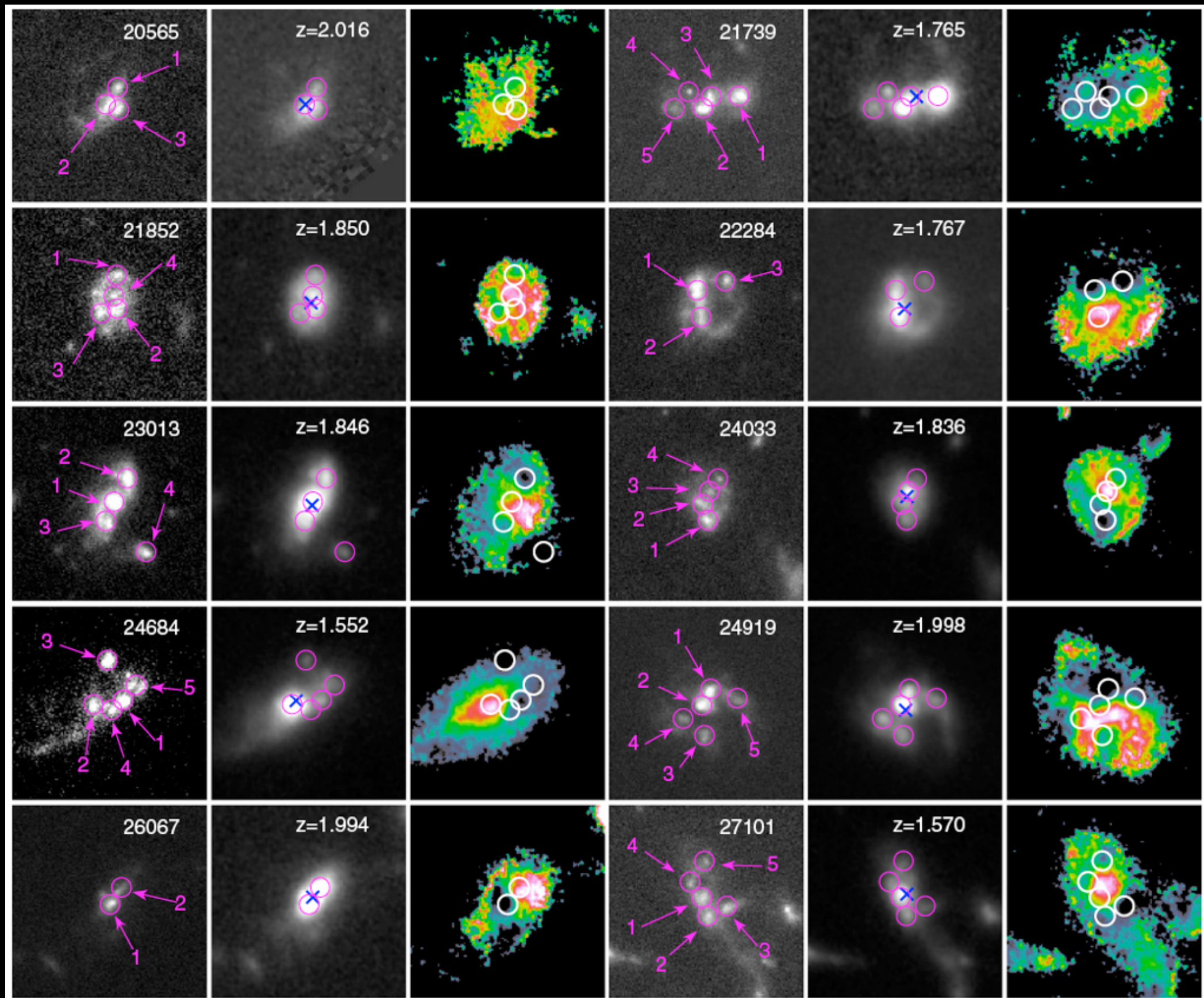
This paper studies the properties of kiloparsec-scale clumps in star-forming galaxies at  $z \sim 2$  through multi-wavelength broadband photometry. A sample of 40 clumps is identified from *Hubble Space Telescope (HST)*/Advanced Camera for Surveys (ACS)  $z$ -band images through auto-detection and visual inspection from 10 galaxies with  $1.5 < z < 2.5$  in the Hubble Ultra Deep Field, where deep and high-resolution *HST*/WFC3 and ACS images enable us to resolve structures of  $z \sim 2$  galaxies down to the kiloparsec scale in the rest-frame UV and optical bands and to detect clumps toward the faint end.

The physical properties of clumps are measured through fitting spatially resolved seven-band (*BVi<sub>z</sub>YJH*) spectral energy distribution to models. On average, the clumps are blue and have similar median rest-frame UV–optical color as the diffuse components of their host galaxies, but the clumps have large scatter in their colors. Although the star formation rate (SFR)–stellar mass relation of galaxies is dominated by the diffuse components, clumps emerge as regions with enhanced specific star formation rates, contributing individually  $\sim 10\%$  and together  $\sim 50\%$  of the SFR of the host galaxies. However, the contributions of clumps to the rest-frame UV/optical luminosity and stellar mass are smaller, typically a few percent individually and  $\sim 20\%$  together. On average, clumps are younger by 0.2 dex and denser by a factor of eight than diffuse components. Clump properties have obvious radial variations in the sense that central clumps are redder, older, more extinguished, denser, and less active on forming stars than outskirts clumps. Our results are broadly consistent with a widely held view that clumps are formed through gravitational instability in gas-rich turbulent disks and would eventually migrate toward galactic centers and coalesce into bulges. Roughly 40% of the galaxies in our sample contain a massive clump that could be identified as a proto-bulge, which seems qualitatively consistent with such a bulge-formation scenario.

The ultra-deep ACS images in the HUDF (Beckwith et al. 2006) cover an area roughly equal to the footprint of the ACS/WFC FOV in the same four filters as the GOODS ACS program, namely F435W (*B*), F606W (*V*), F775W (*i*), and F850LP (*z*) down to a depth of 29.4, 29.8, 29.7, and 29.0 mag ( $5\sigma$ ,  $0''.35$  diameter aperture), respectively. We use the publicly available images, which have been re-binned to the same pixel scale as the GOODS/ACS mosaic, namely  $0''.03 \text{ pixel}^{-1}$  ( $0.6\times$  the original ACS pixel scale).

The WFC3/IR data are from the *HST* Cycle 17 program GO-11563 (PI: G. Illingworth), which aims at complementing the HUDF and the two HUDF05 parallel fields (Oesch et al. 2007) with WFC3/IR images in *Y* (F105W), *J* (F125W), and *H* (F160W) of matching sensitivity,  $\sim 29$  mag (Bouwens et al. 2010; Oesch et al. 2010). Here we use only the first epoch of the images, released in 2009 September, which includes 18 orbits in *Y*, 16 orbits in *J*, and 28 orbits in *H*. We have carried out our independent reduction of the raw data, and after rejecting images affected by persistence in the *J* band, our final stacks reach  $1\sigma$  surface brightness fluctuations of 27.2, 26.6, and 26.3  $\text{mag}_{\text{AB}} \text{ arcsec}^{-2}$  in the three bands, respectively, over an area roughly equal to the footprint of the WFC3/IR camera ( $2''.1 \times 2''.1$ ). We have drizzled the WFC3 images from their original pixel size of  $0''.121 \times 0''.135$  to  $0''.03 \text{ pixel}^{-1}$  to match the scale of the GOODS and HUDF ACS images. Further details on the production of the WFC3 data are given in Koekemoer et al. (2011).

In addition to the *HST*/ACS and WFC3/IR images in the HUDF, the data used in this paper also include panchromatic multi-wavelength photometry obtained as part of the GOODS program, as the HUDF field is embedded in the GOODS south field. The long wavelength baseline of the GOODS photometry enables us to reliably select SFGs based on photometrically derived stellar mass and specific star formation rate (SSFR), while the deep *HST* optical and NIR images allow us to obtain color maps of the galaxies with a resolution of  $\sim 1$  kpc.



Montage of our 10 clumpy star-forming galaxies at  $z \sim 2$ . Each row shows images of two galaxies. For each galaxy, the panels from left to right show the  $z$ -band,  $H$ -band, and  $z-H$  maps. Galaxy IDs are shown in the  $z$ -band images, while redshifts are shown in their  $H$ -band images. Small circles (magenta in the  $z$ -band and  $H$ -band images, and white in the  $z-H$  maps) show the identified clumps. The blue “X”s in the  $H$ -band images show the light-weighted centers.

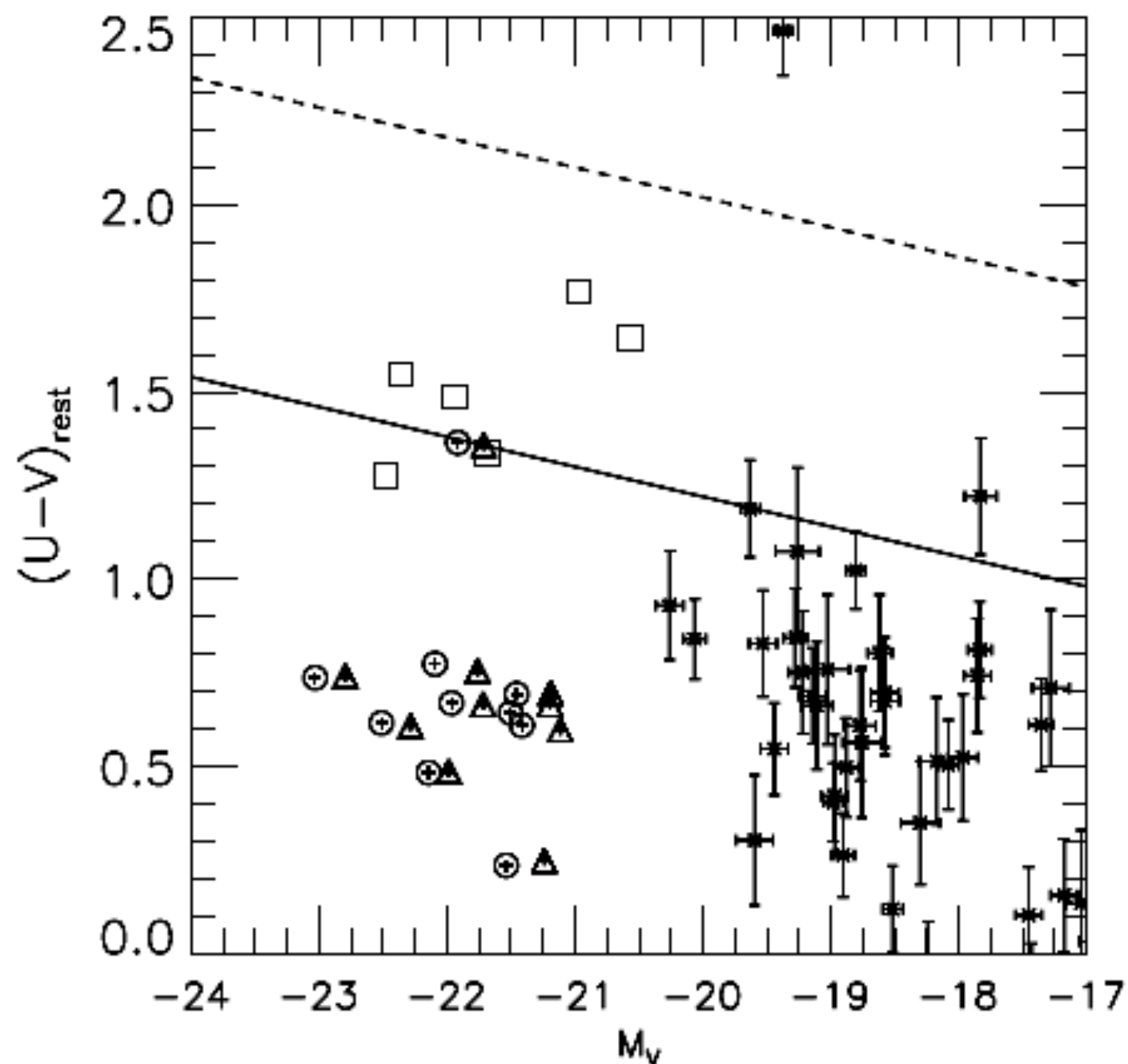


**Figure 2.** Color–magnitude diagram of clumps (star), “disks” (triangle), and host galaxies (circle). Also plotted are six passively evolving galaxies at  $z \sim 2$  (squares) from Guo et al. (2011). We also plot the separation of the red sequence and the blue cloud at  $z = 0$  from Bell et al. (2004) (dashed line). The solid line is the extrapolation of the separation from  $z = 0$  to  $z = 2$  by using the formula of evolution of the separation of Bell et al. (2004).

**Table 2**  
Properties of Clumps and “Disks”

ID 1 Galaxy	ID 2 <sup>a</sup> Clump	$d$ $\frac{d_{\text{proj}}}{r_{\text{kron}}}$	$M_{\text{star}}^{\text{b}}$ $\log(M_{\odot})$	SFR $(M_{\odot} \text{ yr}^{-1})$	$E(B - V)$	Age (Gyr)	$U - V$	$M_V$
20565	1	0.24	$8.80 \pm 0.00$	$3.77 \pm 0.75$	$0.25 \pm 0.05$	$0.20 \pm 0.00$	$0.35 \pm 0.17$	$-18.30 \pm 0.14$
			$8.88 \pm 0.04$	$4.45 \pm 0.89$	$0.25 \pm 0.05$	$0.20 \pm 0.02$	$0.40 \pm 0.14$	$-18.52 \pm 0.12$
			$8.77 \pm 0.00$	$3.49 \pm 0.70$	$0.25 \pm 0.05$	$0.20 \pm 0.00$	$0.32 \pm 0.15$	$-18.20 \pm 0.13$
20565	2	0.01	$9.27 \pm 0.05$	$7.52 \pm 2.04$	$0.30 \pm 0.05$	$0.30 \pm 0.04$	$0.69 \pm 0.14$	$-19.15 \pm 0.12$
			$9.42 \pm 0.03$	$5.40 \pm 2.01$	$0.25 \pm 0.05$	$0.60 \pm 0.05$	$0.68 \pm 0.13$	$-19.25 \pm 0.10$
			$9.15 \pm 0.02$	$5.62 \pm 1.23$	$0.30 \pm 0.05$	$0.30 \pm 0.02$	$0.67 \pm 0.19$	$-18.80 \pm 0.15$
20565	3	0.16	$9.05 \pm 0.06$	$6.72 \pm 2.23$	$0.30 \pm 0.05$	$0.20 \pm 0.03$	$0.61 \pm 0.15$	$-18.77 \pm 0.12$
			$9.11 \pm 0.06$	$7.66 \pm 2.55$	$0.30 \pm 0.05$	$0.20 \pm 0.03$	$0.62 \pm 0.14$	$-18.92 \pm 0.12$
			$9.08 \pm 0.09$	$48.18 \pm 26.62$	$0.30 \pm 0.05$	$0.40 \pm 0.13$	$0.54 \pm 0.20$	$-18.62 \pm 0.18$
20565	D	...	$10.24 \pm 0.03$	$24.62 \pm 4.92$	$0.20 \pm 0.05$	$0.90 \pm 0.07$	$0.66 \pm 0.00$	$-21.20 \pm 0.00$
			$10.28 \pm 0.05$	$30.45 \pm 6.09$	$0.20 \pm 0.05$	$0.60 \pm 0.06$	$0.64 \pm 0.00$	$-21.50 \pm 0.00$
			$10.31 \pm 0.05$	$32.69 \pm 6.54$	$0.20 \pm 0.05$	$0.60 \pm 0.06$	$0.65 \pm 0.00$	$-21.59 \pm 0.00$
21739	1	0.25	$8.97 \pm 0.04$	$5.52 \pm 1.10$	$0.20 \pm 0.05$	$0.20 \pm 0.02$	$0.40 \pm 0.11$	$-18.98 \pm 0.08$
			$9.03 \pm 0.03$	$6.37 \pm 1.42$	$0.20 \pm 0.05$	$0.20 \pm 0.02$	$0.38 \pm 0.10$	$-19.11 \pm 0.07$
			$8.86 \pm 0.04$	$4.33 \pm 0.87$	$0.20 \pm 0.05$	$0.20 \pm 0.02$	$0.41 \pm 0.12$	$-18.71 \pm 0.10$
21739	2	0.22	$8.16 \pm 0.00$	$14.84 \pm 2.97$	$0.25 \pm 0.05$	$0.01 \pm 0.00$	$0.12 \pm 0.11$	$-18.52 \pm 0.07$
			$8.23 \pm 0.00$	$17.36 \pm 3.47$	$0.25 \pm 0.05$	$0.01 \pm 0.00$	$0.14 \pm 0.09$	$-18.71 \pm 0.07$
			$8.12 \pm 0.00$	$13.47 \pm 2.69$	$0.25 \pm 0.05$	$0.01 \pm 0.00$	$0.03 \pm 0.12$	$-18.35 \pm 0.10$
21739	3	0.07	$7.97 \pm 0.29$	$9.51 \pm 2.38$	$0.20 \pm 0.06$	$0.01 \pm 0.01$	$-0.04 \pm 0.13$	$-18.24 \pm 0.10$
			$8.65 \pm 0.07$	$1.77 \pm 0.45$	$0.05 \pm 0.05$	$0.30 \pm 0.08$	$0.01 \pm 0.10$	$-18.49 \pm 0.08$
			$7.87 \pm 0.00$	$7.53 \pm 1.51$	$0.20 \pm 0.05$	$0.01 \pm 0.00$	$-0.08 \pm 0.18$	$-17.95 \pm 0.14$
21739	4	0.34	$8.09 \pm 0.02$	$0.50 \pm 0.10$	$0.05 \pm 0.05$	$0.30 \pm 0.03$	$0.15 \pm 0.17$	$-17.18 \pm 0.10$
			$8.27 \pm 0.07$	$0.61 \pm 0.12$	$0.00 \pm 0.05$	$0.20 \pm 0.03$	$0.19 \pm 0.09$	$-17.73 \pm 0.07$
			$8.30 \pm 0.05$	$0.49 \pm 0.10$	$0.05 \pm 0.05$	$0.50 \pm 0.06$	$0.24 \pm 0.14$	$-17.31 \pm 0.10$
21739	5	0.52	$7.74 \pm 0.10$	$0.70 \pm 0.51$	$0.05 \pm 0.05$	$0.09 \pm 0.03$	$0.13 \pm 0.18$	$-17.04 \pm 0.13$
			$8.19 \pm 0.01$	$0.92 \pm 0.18$	$0.05 \pm 0.05$	$0.20 \pm 0.00$	$0.18 \pm 0.11$	$-17.65 \pm 0.09$
			$8.00 \pm 0.01$	$0.60 \pm 0.12$	$0.05 \pm 0.05$	$0.20 \pm 0.00$	$0.20 \pm 0.15$	$-17.18 \pm 0.12$
21739	D	...	$9.80 \pm 0.04$	$25.18 \pm 5.04$	$0.10 \pm 0.05$	$0.30 \pm 0.05$	$0.25 \pm 0.00$	$-21.24 \pm 0.00$
			$9.92 \pm 0.02$	$33.64 \pm 6.73$	$0.10 \pm 0.05$	$0.30 \pm 0.03$	$0.23 \pm 0.00$	$-21.54 \pm 0.00$
			$9.96 \pm 0.02$	$36.81 \pm 7.36$	$0.10 \pm 0.05$	$0.30 \pm 0.03$	$0.24 \pm 0.00$	$-21.64 \pm 0.00$

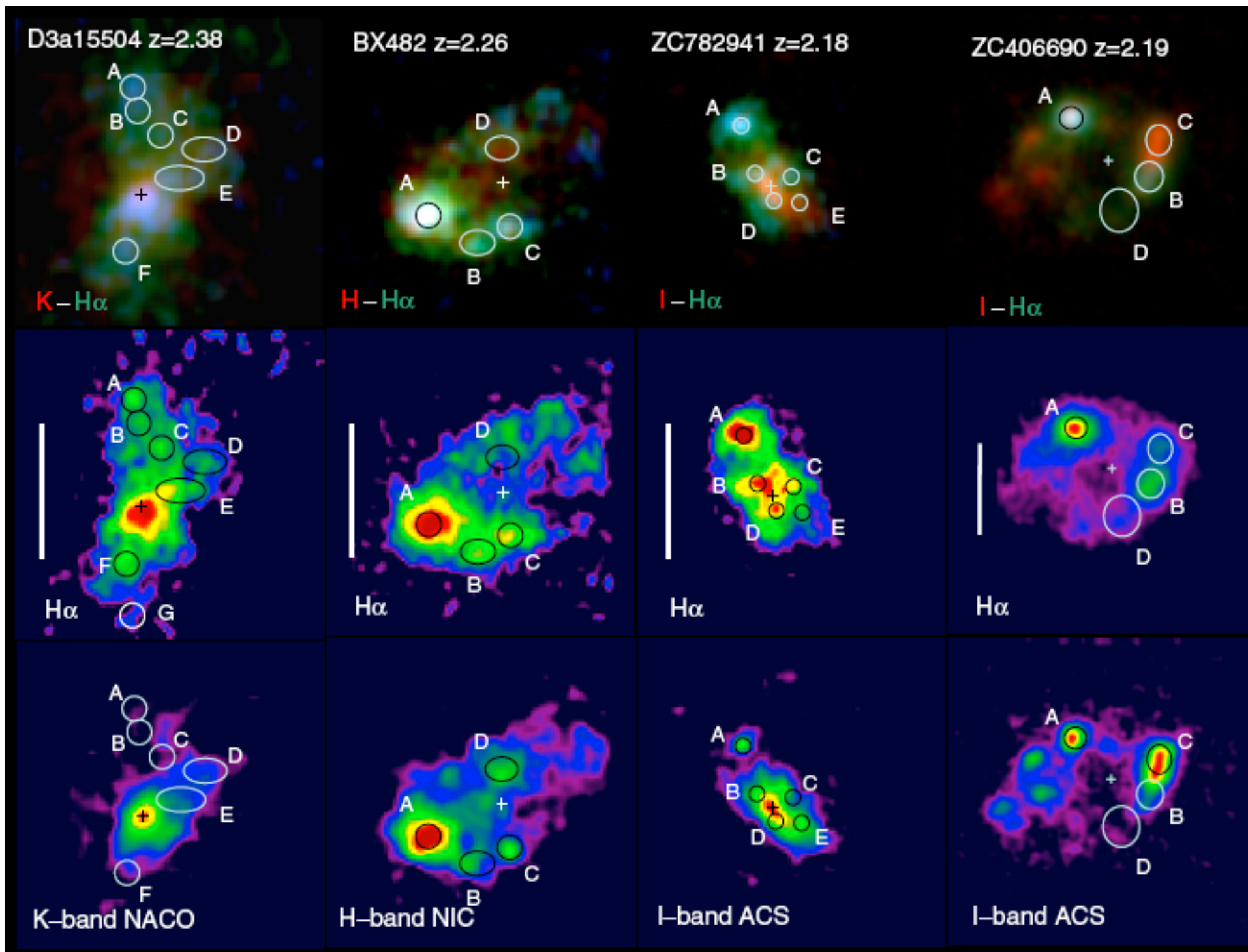
We have studied the properties of giant star-forming clumps in five  $z \sim 2$  star-forming disks with deep SINFONI AO spectroscopy at the ESO VLT. The clumps reside in disk regions where the Toomre  $Q$ -parameter is below unity, consistent with their being bound and having formed from gravitational instability.

Broad H $\alpha$ /[N II] line wings demonstrate that the clumps are launching sites of powerful outflows. The inferred outflow rates are comparable to or exceed the star formation rates, in one case by a factor of eight. Typical clumps may lose a fraction of their original gas by feedback in a few hundred million years, allowing them to migrate into the center. The most active clumps may lose much of their mass and disrupt in the disk.

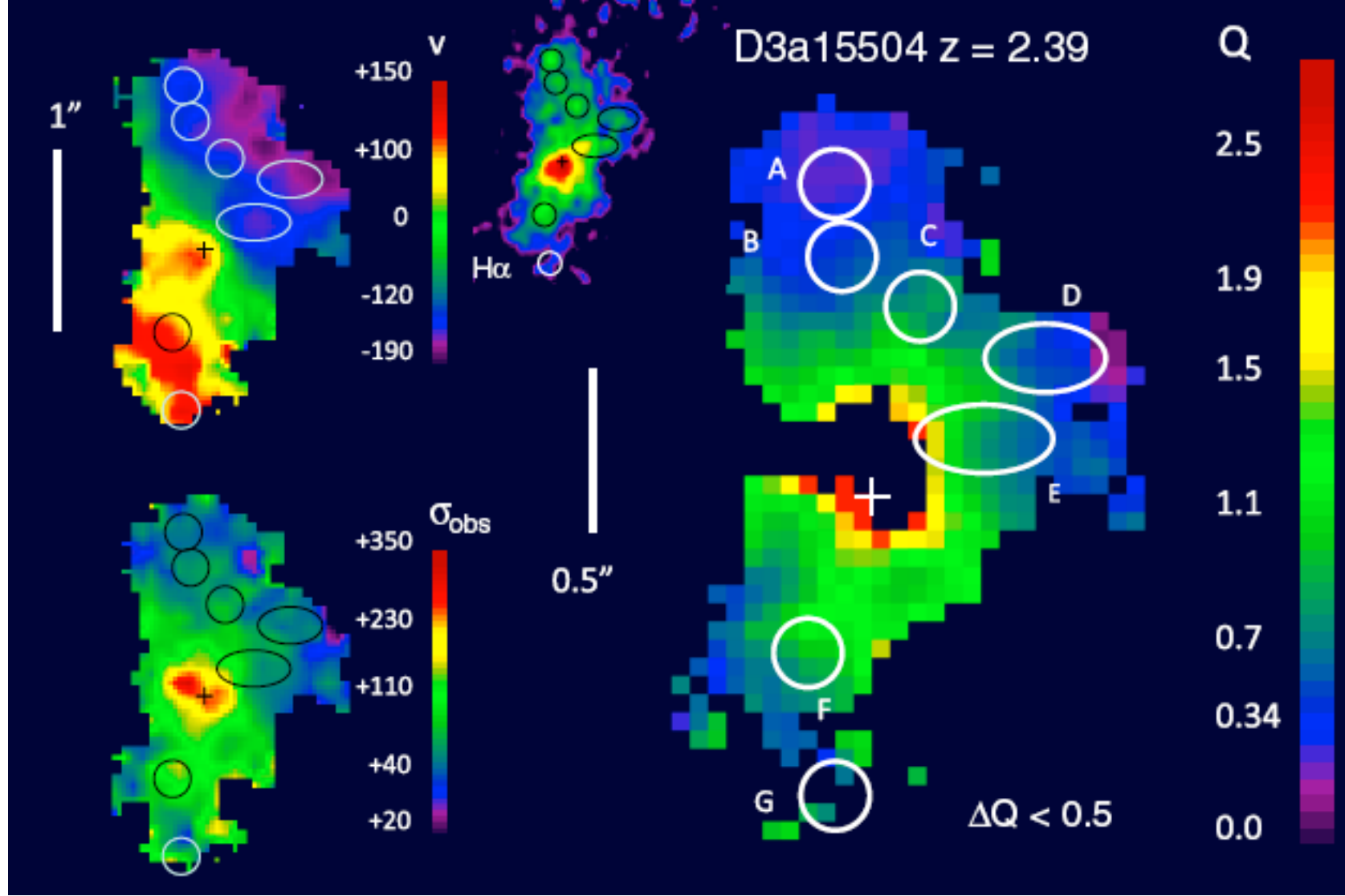
The clumps leave a modest imprint on the gas kinematics. Velocity gradients across the clumps are 10-40 km s $^{-1}$  kpc $^{-1}$ , similar to the galactic rotation gradients. Given beam smearing and clump sizes, these gradients may be consistent with significant rotational support in typical clumps.

Extreme clumps may not be rotationally supported; either they are not virialized or they are predominantly pressure supported. The velocity dispersion is spatially rather constant and increases only weakly with star formation surface density.

The large velocity dispersions may be driven by the release of gravitational energy, either at the outer disk/accreting streams interface, and/or by the clump migration within the disk. Spatial variations in the inferred gas phase oxygen abundance are broadly consistent with inside-out growing disks, and/or with inward migration of the clumps.



FWHM  $\sim 0.2 H\alpha$  and rest-frame UV/optical continuum images of four massive luminous  $z \sim 2$  SFGs. All maps have been re-binned to 0.025 pixels. Top row: three-color composites of integrated  $H\alpha$  line emission (red), and continuum (blue-green) images, along with the most prominent clumps identified by labels A, B, . . . Middle: integrated SINFONI  $H\alpha$  emission. All four images are on the same angular scale, with the white vertical bar marking 1 ( $\sim 8.4$  kpc). Bottom. HST NIC  $H$ -band, ACS I-band, or NACO-VLT AO Ks-band images of the program galaxies, at about the same resolution as the SINFONI  $H\alpha$  maps. The color scale is linear and autoscaled.



H $\alpha$  Gaussian fit velocities (top left), H $\alpha$  Gaussian fit dispersion (bottom left), and inferred Toomre  $Q$ -parameter (right, Equation (2)) for D3a15504. Shown in the top center is also the map of H $\alpha$ -integrated flux from Figure 2. The locations of the main clumps (Figure 1) found in the individual velocity channel maps are denoted by circles/ellipses. The H $\alpha$ , velocity, and velocity dispersion maps (resolution 0.18 FWHM) were re-binned to 0.025 pixels. For construction of the  $Q$ -map, the data were smoothed to 0.25 FWHM. The typical uncertainties in the  $Q$ -values are  $\pm 0.05$  to  $\pm 0.3$  ( $1\sigma$ ) throughout most of the disk of D3a15504.

We estimated molecular surface densities (and masses, including a 36% helium contribution) from Equation (8) of Kennicutt et al. (2007), modified for the Chabrier IMF used here,

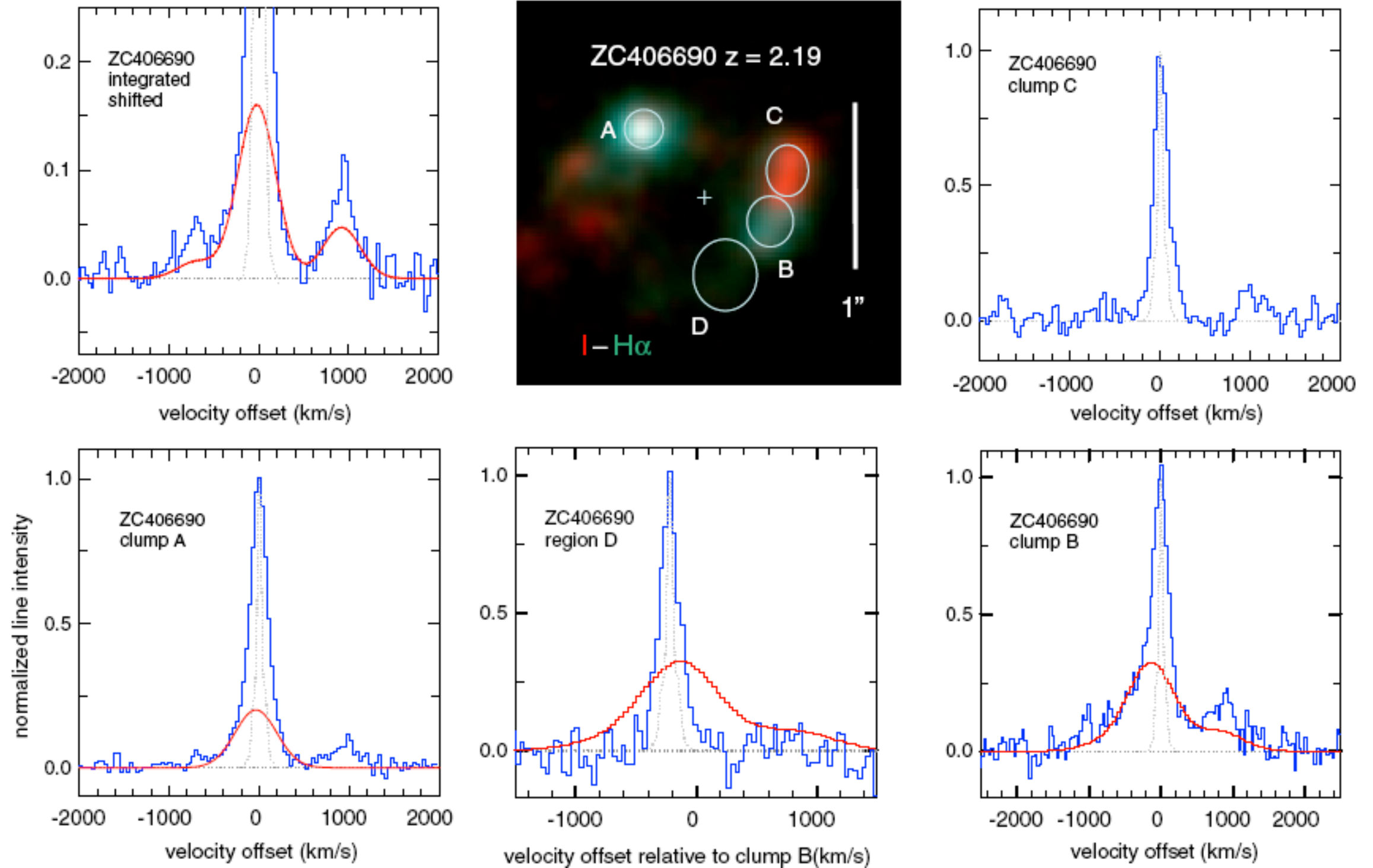
$$\log \left( \frac{\Sigma_{\text{mol-gas}}}{M_{\odot} \text{pc}^{-2}} \right) = 0.73 \log \left( \frac{\Sigma_{\text{star-form}}}{M_{\odot} \text{yr}^{-1} \text{kpc}^{-2}} \right) + 2.91. \quad (2)$$

Equation (2) is based on H $\alpha$ , 24  $\mu\text{m}$ , and CO observations of M51 and is similar to results for larger samples of  $z \sim 0$  SFGs (e.g., Equation (4) in Kennicutt 1998a, and Figure 4 of Genzel et al. 2010). It has the added advantage

$$\begin{aligned} Q_{\text{gas}} &= \frac{\sigma_0 \kappa}{\pi G \Sigma_{\text{gas}}} = \left( \frac{\sigma_0}{v_c} \right) \left( \frac{a (v_c^2 R_{\text{disk}} / G)}{\pi R_{\text{disk}}^2 \Sigma_{\text{gas}}} \right) \\ &= \left( \frac{\sigma_0}{v_c} \right) \left( \frac{a M_{\text{tot}}}{M_{\text{gas}}} \right) = \left( \frac{\sigma_0}{v_c} \right) \left( \frac{a}{f_{\text{gas}}} \right). \end{aligned}$$

Here the constant  $a$  takes on the value of 1,  $\sqrt{2}$ ,  $\sqrt{3}$ , and 2 for a Keplerian, constant rotation velocity, uniform density and solid body disk;  $f_{\text{gas}}$  is the gas fraction within  $R_{\text{disk}}$ . If the disk consists of molecular (H $_2$  + He), atomic (H I + He), and stellar (\*) components,  $Q_{\text{tot}}^{-1} = Q_{\text{H}_2}^{-1} + Q_{\text{H I}}^{-1} + Q_{\text{*}}^{-1}$  if all components have similar velocity dispersions. If there is a (young) stellar

## Evidence for Powerful Outflows on Clump Scales



Our data provide for the first time direct evidence for powerful outflows on the scale of individual star-forming clumps. Figures 7 and 8 show extracted spectral profiles for individual bright clumps, as well as for the entire galaxy in Q1623-BX599 and ZC400690.

the prominent clumps A and B in ZC406690 exhibit blue line wings extending 500 and 1000 km s<sup>-1</sup> half-width at zero power (HWZP) from line center

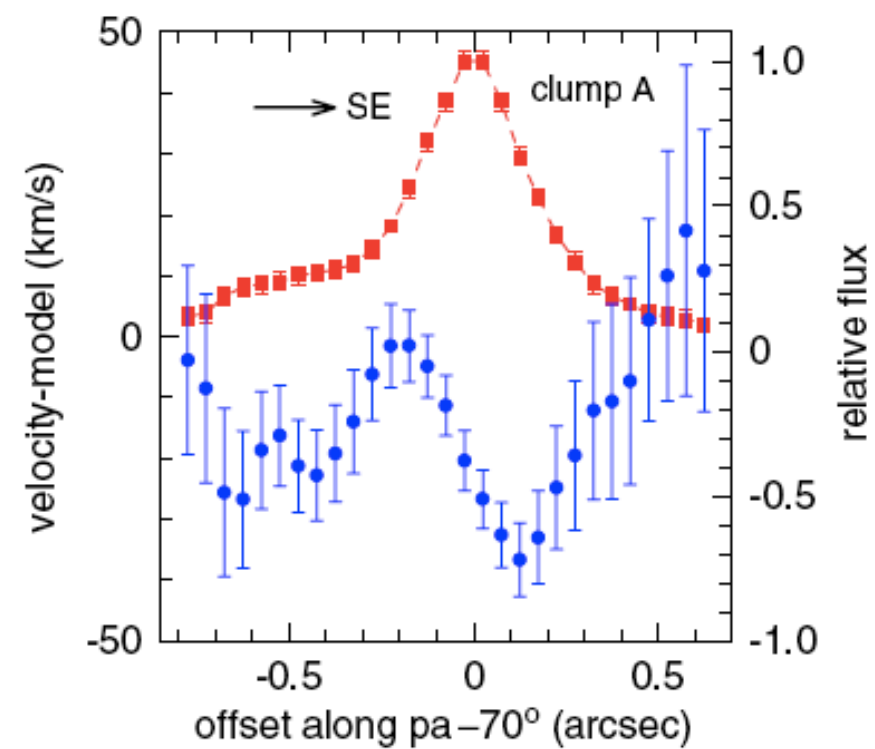
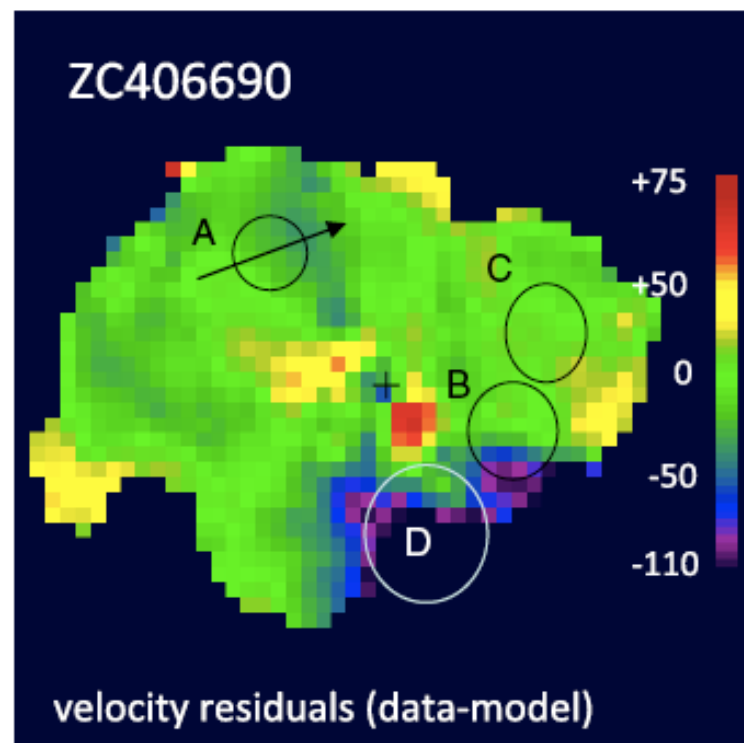
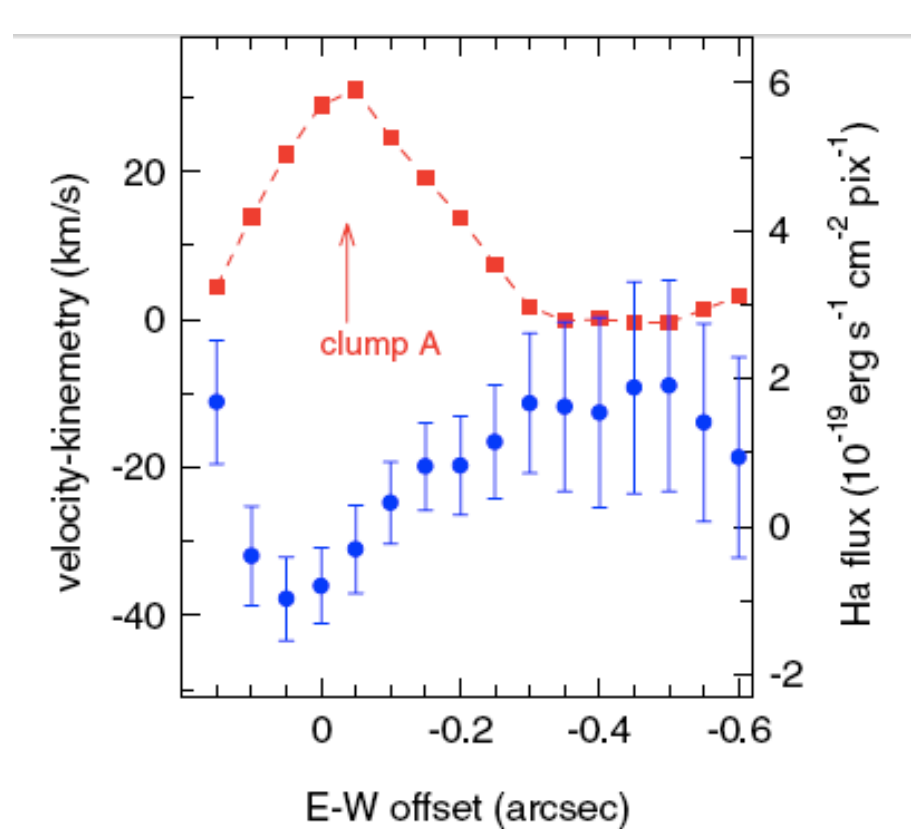
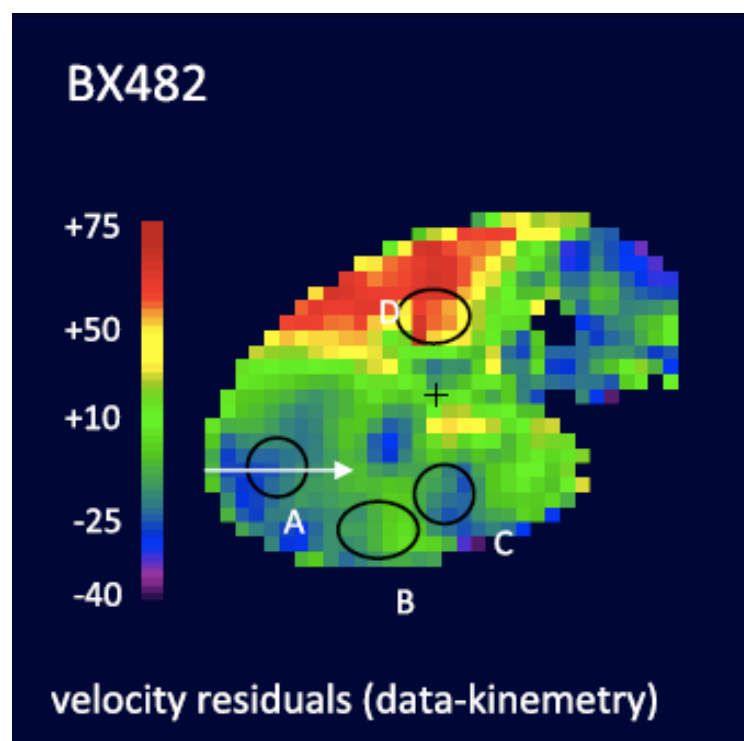
amore symmetric, broad component (FWHM 1000 km s<sup>-1</sup>, HWZP  $\sim$  1000 km s<sup>-1</sup>) is seen in the integrated spectrum

## *Are the Clumps Rotationally Supported?*

Most of the available numerical simulations of the  $z > 1$  gas-rich disks predict that the gravitationally unstable clumps contract, spin-up, and may approach a Jeans equilibrium with half or more of the support in rotation.

We have explored the evidence for rotation in our data by determining the velocity gradients across clumps in the “raw” and “residual” velocity maps. Figures 11 and 12 show the residual velocity distributions in BX482, ZC406690, and D3a15504, after subtracting (by kinemetry or modeling) the large-scale velocity gradients caused by the overall galaxy rotation. Clump rotation should show up as a local gradient in these residual maps. If the clumps originally have a similar angular momentum direction as the galaxy, their rotation should be prograde.

Velocity gradients are indeed present in the velocity maps across the clumps. In the “raw” maps, they are on average comparable in magnitude and sign ( $\delta_{\text{raw}} = \frac{(v_{\text{max}} - v_{\text{min}})_{\text{raw}}}{2 \sin(i) R_{\text{clump}}} \sim 30(\pm 11) \text{ km s}^{-1} \text{ kpc}^{-1}$ ) to the large-scale velocity gradients across the galaxies but there are no large *additional* local gradients. In D3a15504, caution is warranted as the largest gradients (through clumps C, E, and F) may also be interpreted as large-scale, radial streaming of the circumnuclear gas in a barred potential, as discussed in Genzel et al. (2006). After subtraction of the large-scale velocity gradients from galaxy rotation, the inclination corrected “residual” velocity gradients typically are  $\delta_{\text{residual}} = \frac{(v_{\text{max}} - v_{\text{min}})_{\text{residual}}}{2 \sin(i) R_{\text{clump}}} \sim \pm 15(\pm 5) \text{ km s}^{-1} \text{ kpc}^{-1}$ . These residual gradients are often retrograde (negative sign in row 31 of Table 2).



Velocity residual maps and position–velocity residual cuts across the brightest clump A in BX482 (top) and ZC406690 (bottom). The left panels are the residual maps (velocity (data) minus velocity (model or kinemetry)), the right panels give position–velocity residual (and  $\pm 1\sigma$  errors) cross-cuts across the brightest clumps in each galaxy, along the direction of the galaxy’s maximum velocity gradient (line of nodes). The red points and dashed curve denote the H $\alpha$  flux (right vertical axis) and the blue points and continuous curve denote the residual velocity (left vertical axis).